AGU PUBLICATIONS

JGR

Journal of Geophysical Research: Space Physics

RESEARCH ARTICLE
10.1002/2015JA021502

Key Points:
- Lithosphere-atmosphere-ionosphere coupling
- Characteristics of ionospheric response of Nepal earthquake
- Imaging the Rayleigh wave propagation from ionospheric response induced by Nepal earthquake

Correspondence to:
C. D. Reddy,
cdreddy@iigs.iigm.res.in

Citation:
Reddy, C. D., and G. K. Seemala (2015), Two-mode ionospheric response and Rayleigh wave group velocity distribution reckoned from GPS measurement following M_w 7.8 Nepal earthquake on 25 April 2015, *J. Geophys. Res. Space Physics*, *120*, doi:10.1002/2015JA021502.

Received 26 MAY 2015
Accepted 1 AUG 2015
Accepted article online 6 AUG 2015

Two-mode ionospheric response and Rayleigh wave group velocity distribution reckoned from GPS measurement following M_w 7.8 Nepal earthquake on 25 April 2015

C. D. Reddy[1] and Gopi K. Seemala[1]

[1]Indian Institute of Geomagnetism, Navi Mumbai, India

Abstract The coseismic-induced ionospheric total electron content (TEC) perturbations were analyzed following the M_w 7.8 Nepal earthquake (28.147°N, 84.708°E; depth ~15 km) that occurred on 25 April 2015 at 06:11:26 UTC. The ionospheric response is due to both the modes, i.e., shock acoustic waves (slow mode) and Rayleigh wave induced (fast mode). The continuous Global Positioning System (GPS) data at about 60 sites from various GPS networks have been used in the present study. All the sites within epicentral distance of ~2400 km and 70°–170° azimuth recorded the Rayleigh wave-induced TEC response, while the sites within ~400–2200 km in the same azimuth recorded the response from both the modes. The maximum coseismic-induced peak-to-peak TEC amplitude is ~1.2 total electron content unit, 1 TECU = 10^{16} el m^{-2}. From Hodochron plot, the apparent Rayleigh wave velocity has been determined as ~2400 m/s on the average and the acoustic wave velocity as 1180 m/s, both these waves being discernible beyond ~1200 km of epicentral distance as also evident from Hodochron plot and wavelet spectrographs. We reckoned the Rayleigh wave group velocities using ionospheric response at selected radial pairs of stations and validated. The ionospheric response distribution seen mainly depending on the epicentral distance, satellite geometry, directivity of radiation pattern, and the upper crustal heterogeneity. This study highlights the characteristics of ionospheric response consequent to the 2015 Nepal earthquake.

1. Introduction

Ionospheric disturbances following the large earthquakes have been detected by many researchers [e.g., *Calais et al.*, 2003; *Artru et al.*, 2004; *Liu et al.*, 2006; *Astafyeva et al.*, 2009; *Tsugawa et al.*, 2011; *Saito et al.*, 2011; *Heki*, 2011; *Rolland et al.*, 2011a, 2011b; *Cahyadi and Heki*, 2015; *Sunil et al.*, 2015]. Observations from both ground- and satellite-based advanced radio techniques, such as HF Doppler sounding [*Liu et al.*, 2006; *Artru et al.*, 2004; *Ogawa et al.*, 2012], DEMETER [*Ryu et al.*, 2014], Over-The-Horizon radar [*Occhipinti et al.*, 2010], Faraday rotation measurements using linearly polarized electromagnetic signals from geostationary satellites [*Davies*, 1980], and GPS [*Ducic et al.*, 2003; *Heki*, 2011; *Saito et al.*, 2011] are some of the well-established techniques for monitoring ionospheric plasma perturbations caused by large earthquakes. In particular, the GPS receivers are very handy and affordable and provide total electron content (TEC) measurements, which integrate the electron density perturbations between the surface and satellite; they are sensitive to perturbations occurring at higher altitudes, typically 250 to 350 km, and facilitate measurement of both near- and far-field TEC observations following large earthquakes. The integrated value is called total electron content (TEC) and defined as total electron content unit, 1 TECU = 10^{16} el m^{-2}. GPS-based ionospheric measurement can measure TEC variations smaller than 0.01 TECU that can be approximated to a 1% variation in the F_2 peak electron density, integrated 10 km along the ray [*Ducic et al.*, 2003].

Perevalova et al. [2014], after analyzing seismo-ionospheric response of earthquakes during 1965–2013, demonstrated that only those earthquakes with $M_w \geq 6.5$ will have significant wave response in the ionosphere. The tendency of TEC to be larger for the earthquakes of larger magnitudes was first reported by *Astafyeva et al.* [2013]. Further, they demonstrated that the shallow earthquakes with magnitude M_w 7.2–7.8 (as is the case with 2015 Nepal earthquake of M_w 7.8) cause coseismic perturbations with near-field amplitude of 0.2–0.4 TECU (lasting 4–8 min), while mega earthquakes of ~M_w 9.0 and above produce extremely large perturbations of ~1–3 TECU (lasting 30–40 min). The focal mechanism of the earthquake also plays significant role in earthquake

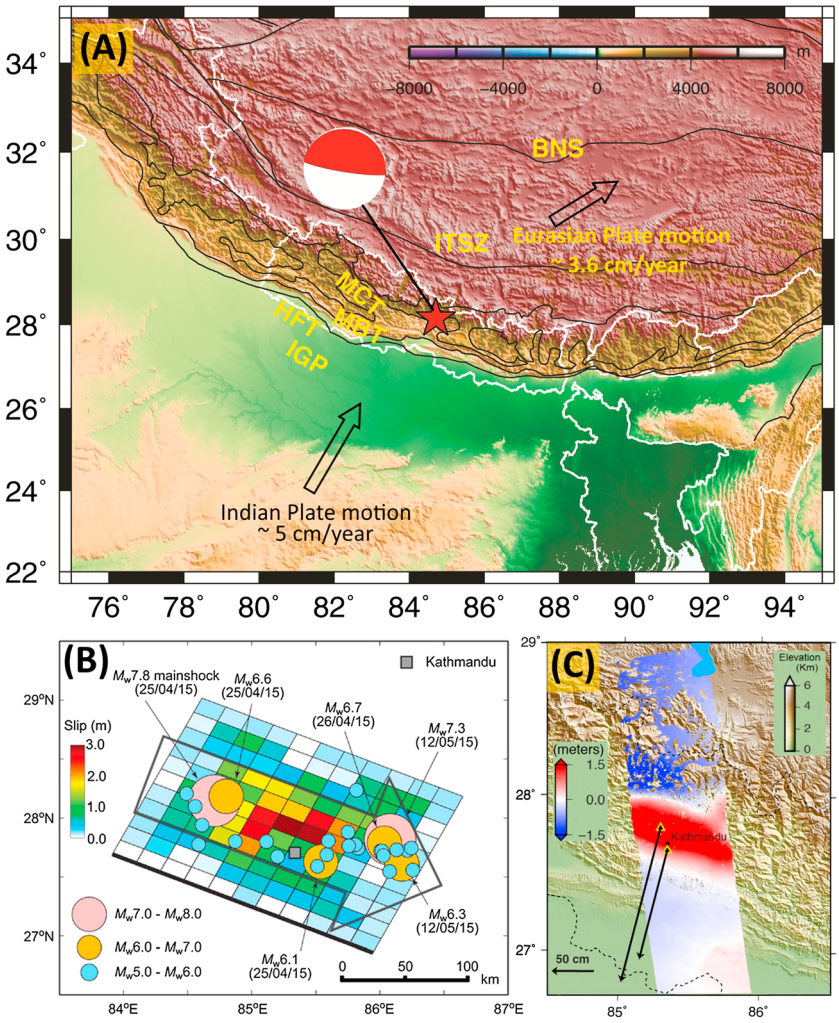

Figure 1. (a) The location of the M_W 7.8 Nepal earthquake on 25 April 2015 is shown by red star. The focal mechanism indicates that the earthquake is purely thrust in nature. (b) Surface slip distribution (an earthquake source model by the U.S. Geological Survey) is shown along with aftershock locations, sized by magnitude, wherein ~3 m slip is seen in epicentral area. The open arrow roughly indicates the rupture direction (south-east). (c) The surface deformation as seen by ALOS-2 satellite images between 21 February and 2 May 2015 (credit: NASA/Jet Propulsion Laboratory-California Institute of Technology (Caltech)/ Japan Aerospace Exploration Agency). The red shaded areas indicate that the land around Kathmandu has moved 1.4 m along line of sight (~1.6 m in vertical direction). The black arrows indicate the horizontal surface displacement as estimated by GPS.

manifestation of the ionospheric response. In addition to the magnitude of the earthquake, the focal depth and earthquake mechanism also count [*Astafyeva and Heki*, 2009]. *Cahyadi and Heki* [2015] provide scaling law, which represents relation between induced TEC and moment magnitude of the earthquake.

It is demonstrated that dense GPS arrays such as Southern California Integrated GPS Network [*Calais et al.*, 2003], Japanese GPS Earth Observation Network (operated by Geographical Survey Institute, Japan [*Sagiya*, 2004; *Ogawa et al.*, 2012]), Sumatra GPS Array [*Sunil et al.*, 2015; *Cahyadi and Heki*, 2013, 2015], and Integrated Plate boundary Observatory Chile provide an opportunity to investigate ionospheric perturbations in most efficient manner. For earthquakes with moderate magnitudes around M_w 6, the signal-to-noise ratio of these perturbations tends to become small and may show up just above the noise level. However, by virtue of the associated waveforms being remarkably coherent over a wide region and the noise being incoherent, it is possible to retrieve the propagation direction and velocity of these perturbations. The imaged ionospheric perturbations from dense GPS arrays could, in principle, be used as a proxy to study the coupling and energy transfer processes in the lithosphere-atmosphere-ionosphere coupled system [*Calais et al.*, 2003]. Unfortunately, as a consequence of the integrated nature of TEC, the sensitivity of GPS to the ionospheric solid

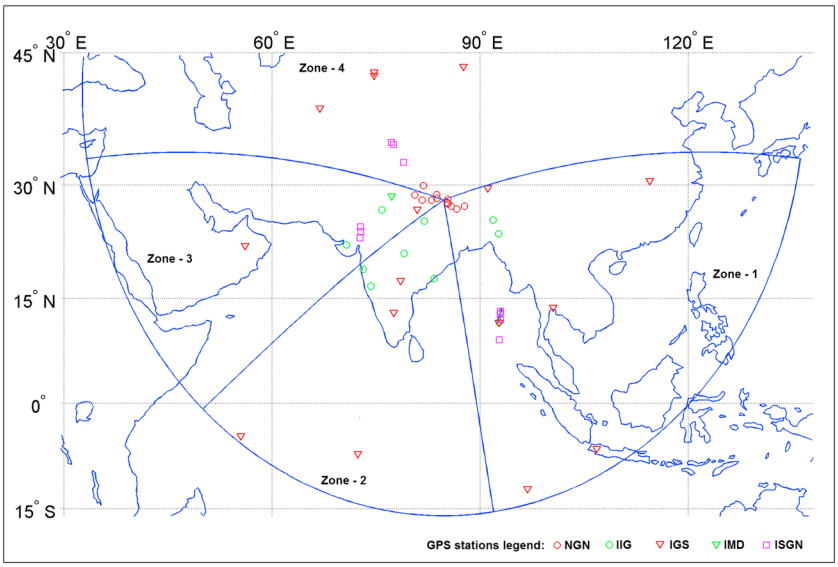

Figure 2. This figure represents GPS sites from various networks indicated by the symbols: red circles (NGN), green circles (IIG), red triangles (IGS), green triangles (IMD), and magenta squares (ISGN). The intersection of four blue lines indicates location of the M_w 7.8 Nepal earthquake on 25 April 2015. We have divided the GPS sites into four zones as indicated, viz., zone 1(eastern), zone 2 (central), zone 3 (western), and zone 4 (northern).

Earth phenomena is limited to large events [*Occhipinti et al.*, 2010]. Numerical modeling of these waveforms [*Rolland et al.*, 2011a; *Kherani et al.*, 2012] will enhance our understating of the possible physical mechanisms and ability in interpreting them.

In addition to the seismic sources, e.g., earthquakes and volcanoes, it should be notable that explosions, e.g., nuclear, chemical [*Row*, 1967], rocket and space shuttle launching [*Ding et al.*, 2014; *Calais and Minster*, 1996], ballistic missiles [*Ozeki and Heki*, 2010], and even asteroids and surface mine blasts, generate significant ionospheric perturbations [*Calais and Minster*, 1996]. Solar events (e.g., coronal mass ejections and solar flares), atmospheric phenomena (e.g., thunderstorms and lightning), and meteorological events (e.g., typhoons and tornadoes) [*Huang et al.*, 1985; *Bishop et al.*, 2006] remain main sources of ionospheric perturbations.

Large earthquakes mainly occur as a consequence of continent-continent collision and plate subduction. The Himalayan Kingdom of Nepal is just located at the boundary between Indian and Eurasian tectonic plates, placing the country highly vulnerable to seismic hazard. As anticipated, M_w 7.8 Nepal earthquake occurred on 25 April 2015 (latitude 28.147°N, longitude 84.708°W; depth ~15 km; 06:11:26 UTC), ~34 km away from Lamjung District of Nepal (also known as the Gorkha earthquake). The earthquake is well recorded by permanent GPS sites in the vicinity. The seismic moment estimated based on the nodal plane (strike = 295°, dip = 10.0°) is 8.1×10^{20} N m. As seen from Figure 1, this earthquake caused ~3 m slip (Figure 1b, modeled) and ~1.8 m surface horizontal displacement (Figure 1c, measured by GPS). Also from Figure 1c, the region around Kathmandu has moved ~1.4 m along line of sight (~1.6 m in vertical direction). The black arrows indicate the horizontal surface displacement as estimated by GPS. The earthquake mainly ruptured SEE region with respect to epicenter and the aftershocks also following this particular trend as indicated by big open arrow shown in Figure 1b. The integrated seismic source model of this earthquake is given by *Yagi and Okuwaki* [2015]. Another large earthquake of M_w 7.3 struck 18 km SE of Kodari (76 km ENE of Kathmandu) on 12 May 2015 at 07:05:19 UTC (Figure 1b). In this study, we mainly explore direct shock acoustic wave (SAW) and the Rayleigh wave-induced (RWI) signatures in the ionosphere consequent to 2015 M_w 7.8 Nepal earthquake, from GPS data collected at ~60 GPS sites in the Indian subcontinent and surrounding region.

2. GPS Data Analysis

We have used GPS data from International Global Navigation Satellite Systems Service (IGS) [*Dow et al.*, 2009], Integrated Seismic and GPS Network (ISGN), Indian Institute of Geomagnetism (IIG) GPS Network, Nepal GPS Network (NGN), and Indian Meteorological Department (IMD) GPS network as shown in Figure 2, whose

Table 1. The GPS Sites Whose Data Considered in This Study are Listed Along With Their Latitude, Longitude, Epicentral Distance, Azimuth, and the Zone in Which They Fall (See Figure 2)

Site	Latitude	Longitude	Distance	Azimuth	Zone	Site	Latitude	Longitude	Distance	Azimuth	Zone
chlm	28.207	85.314	60	83	1	mumb	19.013	73.106	1557	232	2
kkn4	27.801	85.279	68	124	1	kolh	16.677	74.255	1666	222	2
nast	27.657	85.328	82	132	1	chen	13.069	80.246	1740	196	2
sndl	27.385	85.799	137	128	1	iisc	13.021	77.570	1837	205	2
rmte	26.991	86.597	226	124	1	dgar	−7.269	72.370	4155	200	2
tplj	27.352	87.710	308	106	1	seyg	−4.679	55.531	4805	225	2
dhan	23.815	86.444	512	160	1	dnsg	28.345	83.764	95	284	3
lhaz	29.657	91.104	645	73	1	pyut	28.101	82.987	169	269	3
shil	25.563	91.855	765	110	1	npgj	28.117	81.595	305	270	3
aizw	23.731	92.662	934	120	1	lck4	26.912	80.956	395	251	3
impl	24.733	93.929	993	110	1	dngd	28.754	80.582	409	280	3
saih	22.489	92.987	1043	125	1	imdd	28.589	77.221	734	276	3
dgpr	13.177	92.934	1870	151	1	sipu	24.653	72.780	1249	255	3
mbdr	12.907	92.901	1896	152	1	dhar	24.012	72.836	1271	251	3
have	12.009	92.964	1989	153	1	isrr	23.160	72.668	1327	248	3
pbri	11.638	92.712	2016	154	1	rajk	22.294	70.741	1547	248	3
port	11.635	92.738	2017	154	1	yibl	22.186	56.112	2946	263	3
carn	9.161	92.750	2273	157	1	jmsm	28.805	83.743	119	308	4
cusv	13.736	100.534	2290	131	1	smkt	29.969	81.807	347	306	4
jfng	30.516	114.491	2891	77	1	henl	32.779	78.973	753	315	4
bako	−6.490	106.850	4525	145	1	saso	34.921	77.478	1018	320	4
coco	−12.188	96.834	4671	162	1	base	35.179	77.215	1055	320	4
guam	13.589	144.868	6394	91	1	gulm	34.056	74.375	1182	306	4
alh2	25.408	81.936	410	223	2	urum	43.590	87.630	1737	8	4
nagp	21.144	79.046	966	218	2	pol2	42.680	74.694	1850	333	4
visa	17.725	83.322	1167	187	2	chum	42.998	74.751	1878	334	4
hyde	17.417	78.551	1349	209	2	kit3	39.140	66.880	2047	311	4

coordinates and epicentral distances are given in Table 1. As the observed ionospheric response was highly directional, we have categorized these GPS stations into four zones, namely, zone 1 (from azimuth 70° to 170°), zone 2 (from 170° to 235°), zone 3 (235° to 290°), and zone 4 (290° to 20°), all the zones extending up to radius of 5000 km with respect to epicenter. Compounding all these networks, we obtained an excellent GPS data set to study the earthquake-induced ionospheric plasma perturbations. Such dense GPS networks can facilitate, providing 2-D ionospheric response, sufficiently accurate to image the near- and far-field ionospheric perturbations induced by both SAW and RWI.

The calculation of the ionospheric vertical TEC was done independently at all these sites using both code and phase measurements of the two, i.e., L_1 ($f_1 = 1575.42$ mHz) and L_2 ($f_2 = 1227.60$ mHz) frequencies. Thus, we eliminated the effect of clock errors and tropospheric water vapor and estimated the relative values of slant TEC [*Sardón and Zarraoa*, 1997]. Then, the absolute values of TEC are obtained by including the differential satellite biases published by the University of Bern and the receiver bias that is calculated by minimizing the TEC variability between 02:00 and 06:00 LT [*Valladares et al*., 2009; *Seemala and Valladares*, 2011].

Thus, estimated TEC can have high degree of accuracy, i.e., at least 10^{14} el m^{-2} when averaged on a 30 s sampling interval (in this study the GPS data are considered sampled at 30 s interval). Short-term ionospheric perturbations are extracted by applying a band-pass filter 2–10 milli-Hertz (mHz). For representation purpose, we locate the TEC measurement at the intersection of the line of sight and an ionospheric thin layer whose altitude is chosen near the peak of electron density, here at 300 km. These points are referred to as ionospheric piercing points (IPPs). As the GPS TEC technique is strongly dependent on the observation geometry, we considered the geometries for several satellites, viz., PRN 03, PRN 16, PRN 23, PRN 26, and PRN 27. Figure 3 gives the ionospheric response at various permanent GPS sites falling in different zones (see Figure 2). The IGS sites (shown as red triangles in Figure 2) (excluding lck3, hyde, iisc, cusv, and lhas), viz., xian, jfng, kunm, baco, and coco (to east, zone 1); dgar and seyg (to south, zone 2); bhr2, ylbl, and tehn (to west, zone 3); and kit3, pol2, chum, sele, guao, and urum (to north, zone 4) do not show any ionospheric response above noise level.

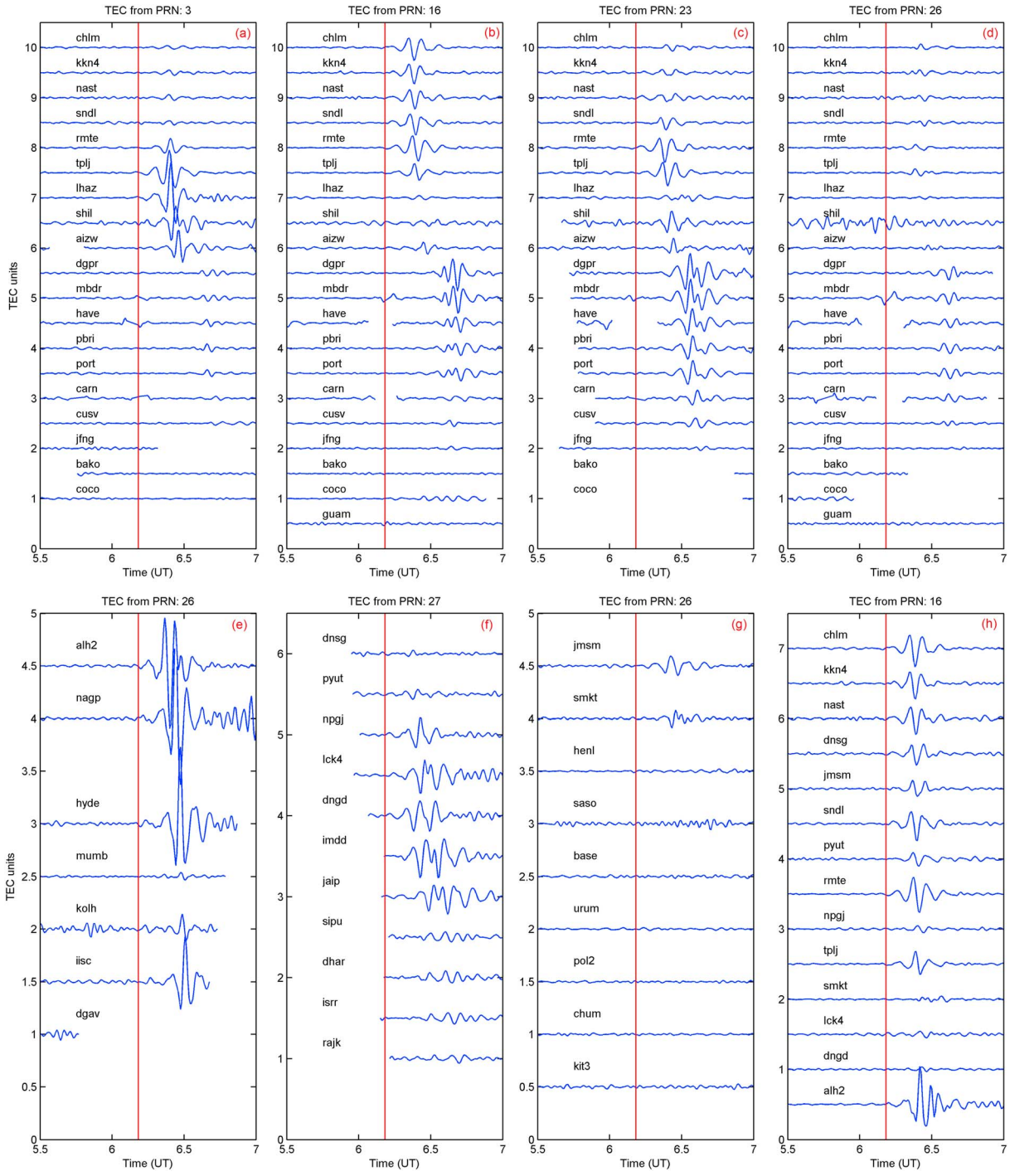

Figure 3. Stacked ionospheric TEC response at various GPS sites (shown in Figure 2) estimated following 2015 Nepal earthquake. (a) PRN 3, (b) PRN 16, (c) PRN 23, and (d) PRN 26, respectively, for the GPS sites in zone 1. (e) PRN 26, (f) PRN 27, (g) PRN 26, and (h) PRN 16 for zone 2, zone 3, zone 4, and Nepal GPS Network, respectively. The vertical red line indicates the time of 25 April 2015 Nepal earthquake. In Figure 3c, it is clearly depicted how the slow mode gradually diminished with increasing epicentral distance and while the fast mode persists as far as at the site cusv which is also clearly portrayed in Hodochron plot in Figure 4 and wavelet spectrographs shown in Figure 5.

As seen in Figure 3, following the 2015 Nepal earthquake, we observed that maximum coseismic ionospheric response is as large as ~1.2 TECU (peak to peak) at stations Lhasa (lhaz—Figure 3a), Allahabad (alh2), Nagpur (nagp), and Hyderabad (hyde) seen in Figure 3e. And the response is observed as far as ~2300 km (e.g., Carnicobar (carn), India; Chulalongkorn (cusv), Thailand), which is 2–3 times above the noise level. It should

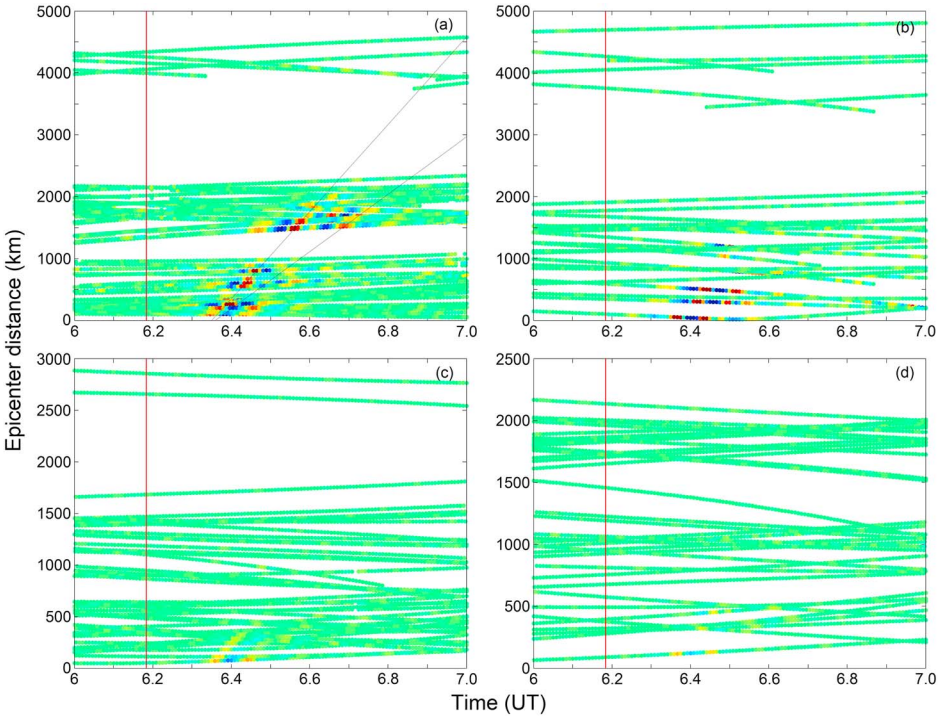

Figure 4. (a) Hodochron plot (travel time diagram) showing variation in vertical TEC at various GPS sites as a function of time and epicentral distance, obtained from PRNs 3, 16, 23, and 26. Linear relationship between travel time and epicentral distance is seen for both shock acoustic waves and Rayleigh wave-induced acoustic waves (shown as thin slant grey lines). Slopes of these slant lines 1180 m/s and 2400 m/s give the average velocity SAW and the RWI, respectively. (b–d) Hodochron plots for zone 2, zone 3, and zone 4 (see Figure 2) for PRNs 3,16, and 27, respectively.

be noted that such magnitude disturbances can be caused by variety of sources [*Pulinets*, 2004]. At times, it is feasible to use geomagnetic and solar indices, viz., *Kp*, *Ap*, *Dst*, S_4, σ_φ, and $F_{10.7}$, to distinguish seismo-ionospheric anomalies from that of geomagnetic and solar activities. However, the best way to check that the observed plasma perturbation is caused by SAW or RWI or by both of them (as is the case in this study) is by using hodochron plots (distance versus time plot) generated for all the PRNs (PRN 3, PRN 16, PRN 23, and PRN 26) as shown in Figure 4. As shown in Figure 4a, pertaining to the hodochron plots for zone 1 stations, there is a clear linear relationship (shown as black lines) between travel time and epicentral distance for both shock acoustic waves and Rayleigh wave-induced acoustic waves. Slope of the slant lines give the average velocities 1180 m/s and 2400 m/s for the SAW and the RWI, respectively. Figures 4b–4d are hodochron plots for zone 2, zone 3, and zone 4 (see Figure 2) for PRNs 3, 16, and 27, respectively; as these zones are not falling in the radiation pattern, this feature is not reflected. These plots allowed estimating the mean Rayleigh wave propagation velocity. It is clearly seen from the linear relationship between travel time and epicentral distance the slopes yielding shock acoustic and Rayleigh wave-induced velocities, 1180 m/s and 2400 m/s, respectively. The 30 s sampling rate of the GPS data is large and may introduce small shifts causing error in estimation of the velocity.

3. Results and Discussion

The M_w 7.8 Nepal earthquake on 25 April 2015 caused ~1.8 m horizontal and ~1.6 m vertical displacement, as part of uplifting, in an area of 120 km^2 around the epicentral region (see Figure 1c). In this scenario we can expect that ionospheric TEC perturbations from low frequency (with velocity 500–1500 m/s) directly generated SAW [*Calais and Minster*, 1995] and RWI by dynamic coupling (with velocity 2000–4000 m/s). In general, the fast-propagating RWI ionospheric response gets superimposed on the slow-propagating acoustic waves, and these two signals, by virtue of distinct velocities, get separated with increase in epicentral distance [*Astafyeva et al.*, 2009]. In this study we see that both the modes (i.e., slow mode ~4 mHz and fast mode ~2.7 mHz) are recorded within the epicentral distance ~400–2200 km and these waves being discernible

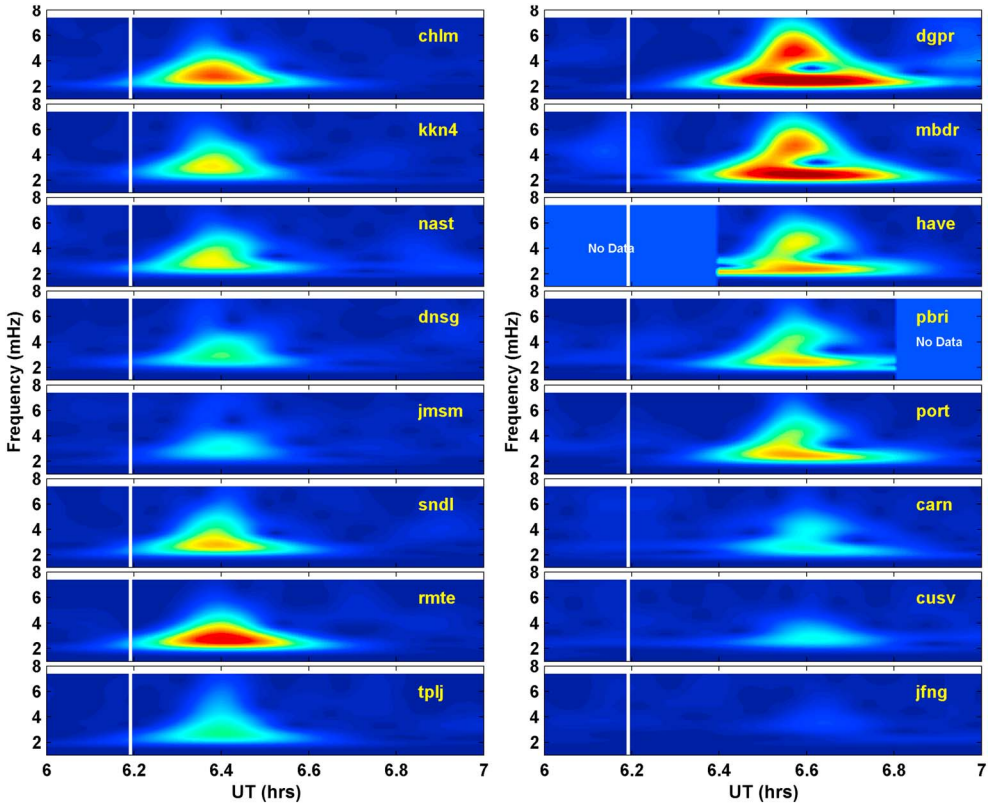

Figure 5. (left) Wavelet spectograms of vertical TEC time series for GPS sites in NGN network and (right) for the selected sites in Andaman arc region (in zone 1). For the Nepal sites, we see the consistent response corresponding to fast mode. In the Andaman arc region, it is very evident that the response is for both the modes (slow and fast) and the slow mode gets diminished with increasing epicentral distance and at the site cusv, only the fast mode sustains. The vertical white line indicates the time of the 2015 Nepal earthquake.

beyond ~1200 km which is also evident from Hodochron plot (Figure 4) and wavelet spectrograms (Figure 5). From Figure 3, it is seen that while the amplitude of ionospheric response due to SAW becomes significant beyond ~400 km (obeying epicentral distance, geomagnetic field influence, etc.), the amplitude due to RWI response is consistent throughout obeying the radiation pattern and "evanescent" rules (e.g., Rayleigh wave amplitudes decay with distance as 1/r).

3.1. The Spatiotemporal Characteristics

As it is seen from Figure 2, many of the GPS sites are located in equatorial ionization anomaly (EIA) region. As a consequence of vertical $E \times B$ drift, this region is characterized by an enhanced electron density in 10°± to 20°± magnetic latitudes at *F* region [e.g., *Anderson*, 1981]. EIA can result a sharp latitudinal TEC gradient equatorward and poleward side, the latter being more intense [*Paul et al*., 2011]. Following 11 April 2012 Indian Ocean earthquake, *Catherine et al*. [2015] appraised the influence of EIA-induced spatial variability of TEC on the amplitude variation. In this study, as seen from Figure 3, in general, the sites in EIA region have pronounced ionospheric response with equatorward and poleward gradient, however subjected various other influencing factors.

As discussed above, the near-field ionospheric response is a consequence of slow mode SAW generated by sudden vertical displacement of the Earth. In this case, the general ionospheric response is manifested as N-shaped [e.g., *Landau and Lifshitz*, 1995; *Astafyeva and Heki*, 2009], with shorter positive and longer negative spreading, as the compression and rarefactions have high and low acoustic wave velocities, respectively. It is better pronounced in the near field whose magnitude is governed by the interplay between the damping with distance and influence of the geomagnetic field inclination at IPPs. On the other hand, the RWI fast mode is caused by a traveling source of dynamic coupling and known to be better pronounced in the far field. As it is seen that the slow component decays faster with the epicentral distance ~1500 km; i.e., the

high-frequency components (~4 mHz herein) attenuate faster than the low-frequency ones (~2.7 mHz herein). These characteristics are clearly seen in Figure 3, particularly for the PRN 23 for the chain for GPS sites between "dgpr" and "jfng."

As seen from the Hodochron plot in Figure 4, the slow mode and fast mode are discernable beyond epicentral distance of ~1200 km. We estimated 1180 m/s and 2400 m/s velocities for slow and fast modes, respectively. But we see a bit of ambiguity in this estimation which may be due to the following: the slow mode propagates with a velocity less than the sound speed and further slows down with distance while the velocity of the fast mode increases with epicentral distance, perplexing the delineation of the slow and fast modes. This separation of slow and fast modes can be clearly observed from the spectrogram of the TEC time series. This exercise has been done for GPS sites in NGN network as shown in Figure 5 (left) and for sites in zone 1 (Figure 5, right). For the Nepal sites, we see the consistent response corresponding to fast mode. In the Andaman arc (zone 1) region, it is very evident that the response is for both the modes (slow and fast) and the slow mode gets diminished with increasing epicentral distance and at the site "cusv," only the fast mode sustains. Also, it can be seen from Figure 5 (left), while the ionospheric response Rayleigh wave is conspicuous, the shock acoustic response is not. This may be due to (i) the SAW response is masked by RWI response hindering its portraying and (ii) in the epicentral area, it is likely that various responses concurrently exist and the response amplitude annihilation is possible (e.g., the seismic *S* waves and Rayleigh wave can arrive at particular location at the same time). However, these above points (i and ii) have to be validated by modeling or simulation.

In isotropic media, the Rayleigh surface wave propagates radically and detected equally in all directions. In our study, we see that the earthquake induced southeast-east (SEE) directed Rayleigh wave radiation emission lobes. In particular, we see very diminished and insignificant amplitudes in western and northern regions of the Indian continent. In particular, we do not see any significant ionospheric response in northern region. The reasons may be (i) it is difficult to understand Rayleigh wave propagation in high hilly terrain (e.g., in the vicinity of Mount Everest); (ii) the Rayleigh wave and *S* wave signatures may not be distinguishable in case both the waves arrive almost simultaneously [*Heki and Ping*, 2005]; (iii) the magnetic field contributes to the northern attenuation, i.e., only detected in a magnetic equatorward direction due to magnetic field inclination [*Heki and Ping*, 2005; *Otsuka et al*., 2006], i.e., in low-latitude regions as is the case in this study, where the magnetic field is perpendicular to the neutral atmosphere velocity and favorable to an efficient coupling with the atmosphere; and (v) location of the IPPs with respect to direction of an emission lobe of the Rayleigh wave radiation which in turn depends on fault azimuth.

The characteristics of the waveform and its amplitude strongly depend on the observation geometry of the GPS satellites (e.g., satellite elevation angle, i.e., 40° provides an efficient detection of RWI ionospheric waves [*Rolland et al*., 2011a]), with disturbance wavefront, the direction of the geomagnetic field (as discussed above) [*Heki and Ping*, 2005; *Afraimovich et al*., 2001], and azimuth of subionospheric point relative to epicenter [*Astafyeva and Heki*, 2009]. Often the epicenter and the actual ground displacement are separated by large distances. These characteristics also can vary with the local time (the signal-to-noise ratio is relatively low at local midafternoon [*Heki and Ping*, 2005], the season, and the level of geomagnetic disturbance [*Afraimovich et al*., 2001]). It is to be noted that the level of geomagnetic disturbances was quiet during the Nepal earthquake on 25 April 2015 with *Kp* index varied from 0 to 1. While some of these aspects are addressed by *Cahyadi and Heki* [2015] using 21 large earthquakes having M_w 6.6–9.2, TEC response amplitude during quiet and disturbed geomagnetic conditions have been compiled by *Perevalova et al*. [2014].

3.2. Imaging the Rayleigh Wave Group Velocity

The TEC measurements from dense GPS networks can provide a direct measurement of the local Rayleigh wave group velocity by imaging the wavefront in space and time which in turn can be used for lithospheric tomography [*Ducic et al*., 2003]. In order to image the Rayleigh group velocity, we considered the RWI ionospheric response at various permanent GPS sites. Using arrival times of the waveforms, we determined the apparent Rayleigh wave group velocities by cross correlation between a set of pairs of GPS sites (IPPs). We ensured that the pairs of GPS sites (nast-alh2, prn-16; nast-lck4, prn-16; nast-shil, prn-23; smkt-henl, prn-27; alh2-nagp, prn-26; lck4-isrr, prn-27; dgpr-carn, prn-23; lck4-jaip, 27; and iisr-rajk, prn-26) were falling approximately on radial lines. It should be noted that these estimates do not depend on amplitude of the ionospheric response.

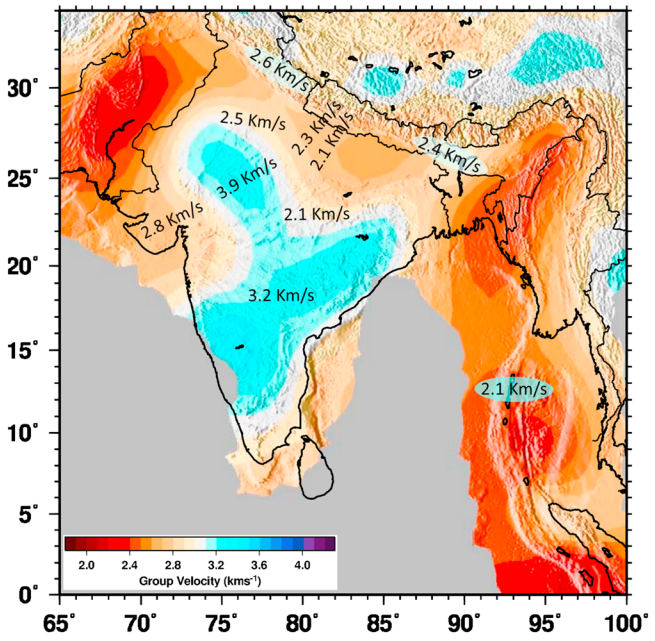

Figure 6. The Rayleigh group velocities calculated in this study are marked (in digits km/s) on the corresponding region for comparison with Rayleigh wave fundamental group velocity for 10 s obtained (contour color map) by *Acton et al.* [2010]. The pairs of stations (in radial direction) used are nast-alh2, prn-16; nast-lck4, prn-16; nast-shil, prn-23; smkt-henl, prn-27; alh2-nagp, prn-26; lck4-isrr, prn-27; dgpr-carn, prn-23; lck4-jaip, prn-27; and iisr-rajk, prn-26.

The obtained mean group velocity of 2.4 km/s is validated by a global map of Rayleigh group velocities [*Larson and Ekstrom*, 2001; *Ma et al.*, 2014]. On the other hand, we have Rayleigh group velocity distribution for Indian subcontinent (for 10–70 s period) estimated from 1001 [*Mitra et al.*, 2006] and 4054 [*Acton et al.*, 2010] source-receiver paths. Because of the dense station coverage, particularly in peninsular India, these results have substantially higher lateral resolution when compared to global and regional group velocity studies [e.g., *Larson and Ekstrom*, 2001; *Ma et al.*, 2014]. Our average group velocity estimated for Bengal Bain, NE, and Andaman region has a very good comparison with that of *Acton et al.* [2010] (see Figure 6). These regions show extremely low velocities due to the thick sediment blanket [*Mitra et al.*, 2006; *Acton et al.*, 2010]. On the other hand, Indian shield is characterized by high group velocities and comparatively lower velocities beneath the Indo-Gangetic Plains (due to alluvium) and the Himalaya region (due to the thickened crust). Any discrepancies in the comparison mainly arise due to the factors such as (i) mainly due to sampling interval (for 30 s, the waveform corresponds to a group delay of about 120 km propagation, i.e., 4 km/s × 30 s); (ii) the horizontal heterogeneities in the ionosphere; and (iii) IPP projection on to the ground, assumption of 350 km IPP height [*Rama Rao et al.*, 2006]. Two-mode (slow and fast) propagation of coseismic ionosphere disturbances [*Astafyeva et al.*, 2009], as is the case herein, complicates the delineation of the phase arrival timings. Nevertheless, estimation of Rayleigh wave velocity distribution from seismo-ionospheric response is an important step in ionospheric seismology, and in this context, we refer the work of *Occhipinti et al.* [2010] titled "the radar that wanted to be a seismometer," whereby the radar can be a GPS receiver as well.

4. Conclusions

The GPS networks in the Indian subcontinent facilitated study of SAW (slow mode, ~4 mHz) and RWI ionospheric response (fast mode, ~2.7 mHz) following M_w 7.8 Nepal earthquake on 25 April 2015. The maximum coseismic-induced peak-to-peak TEC amplitude is ~1.2 TECU, and GPS sites recorded this response as far as ~2400 km. The velocities of slow and fast modes are estimated as ~1180 m/s and Rayleigh ~2400 m/s, respectively, both these modes being discernible beyond ~1200 km of epicentral distance. We also estimated the Rayleigh group velocity distribution and validated with ground seismic-derived results, thereby demonstrating the sensitivity of the ionosphere to solid Earth phenomena. This is construed as one way of providing authentication of our seismo-ionospheric TEC response. The GPS data at 1 Hz sampling rates or higher can image the seismo-ionospheric perturbation more accurately. It is feasible that these data can be used to obtain the same over the oceans so as to enhance our understanding in the lithosphere beneath the oceans. Further, the ionospheric perturbations carry traceable information about the earthquake itself that generated them. Therefore, understanding the connection between the solid Earth (lithosphere), atmospheric, and seismo-ionospheric perturbations can potentially augment the earthquake reporting systems and considered utmost importance for mitigation of seismic risk.

Acknowledgments
Authors thank Shailesh Nayak (Secretary, MoES), Satheesh C. Shenoi (Director, INCOIS), T. Srinivas Kumar, V. Venu Gopal Rao, M.V. Sunanda, S. Moinudeen, and ISGN team at INCOIS for providing the GPS data. We thank P.S. Sunil, S. Tulasi Ram, M. Ravi Kumar, and all our observatory staff for maintaining the GPS receivers and providing the GPS data for this event and support. We thank Pierdavide Coïsson (Institut de Physique du Globe de Paris, France) for going through this manuscript and giving his valuable suggestions. We thank D.S. Ramesh (Director, IIG) for giving impetus in ionospheric seismology studies in our institute. The authors also acknowledge the following agencies/institutes (with hyperlinks or e-mail) for making the GPS data available: ISGN (www.isgn.gov.in/ISGN), IGS (www.igs.org/network), IMD (www.imd.gov.in), NGN (www.unavco.org), and IIG (iigm.res.in). The authors thank the reviewers for their valuable comments and suggestions for improving this paper.

Alan Rodger thanks the reviewers for their assistance in evaluating this paper.

References

Acton, C. E., K. Priestley, V. K. Gaur, and S. S. Rai (2010), Group velocity tomography of the Indo Eurasian collision zone, *J. Geophys. Res.*, *115*, B12335, doi:10.1029/2009JB007021.

Afraimovich, E. L., N. P. Perevalova, A. V. Plotnikov, and A. M. Uralov (2001), The shock-acoustic waves generated by the earthquakes, *Ann. Geophys.*, *19*(4), 395–409.

Anderson, D. N. (1981), Modeling the ambient, low latitude *F*-region ionosphere—A review, *J. Atmos. Terr. Phys.*, *43*, 753–762.

Artru, J., T. Farges, and P. Lognonne (2004), Acoustic waves generated from seismic surface waves: Propagation properties determined from Doppler sounding observations and normal-mode modeling, *Geophys. J. Int.*, *158*, 1067–1077.

Astafyeva, E., and K. Heki (2009), Dependence of wave form of near-field coseismic ionospheric disturbances on focal mechanisms, *Earth Planet Space*, *61*, 939–943.

Astafyeva, E., K. Heki, V. Kiryushkin, E. L. Afraimovich, and S. Shalimov (2009), Two-mode long-distance propagation of coseismic ionosphere disturbances, *J. Geophys. Res.*, *114*, A10307, doi:10.1029/2008JA013853.

Astafyeva, E., S. Shalimov, E. Olshanskaya, and P. Lognonne (2013), Ionospheric response to earthquakes of different magnitudes: Larger quakes perturb the ionosphere stronger and longer, *Geophys. Res. Lett.*, *40*, 1675–1681, doi:10.1002/grl.50398.

Bishop, R. L., N. Aponte, G. D. Earle, M. Sulzer, M. F. Larsen, and G. S. Peng (2006), Arecibo observations of ionospheric perturbations associated with the passage of Tropical Storm Odette, *J. Geophys. Res.*, *111*, A1132, doi:10.1029/2006JA011668.

Cahyadi, M. N., and K. Heki (2013), Ionospheric disturbances of the 2007 Bengkulu and the 2005 Nias earthquakes, Sumatra, observed with a regional GPS network, *J. Geophys. Res. Space Physics*, *118*, 1–11, doi:10.1002/jgra.50208.

Cahyadi, M. N., and K. Heki (2015), Coseismic ionospheric disturbance of the large strike-slip earthquakes in North Sumatra in 2012: M_w dependence of the disturbance amplitudes, *Geophys. J. Int.*, *200*, 116–129.

Calais, E., and J. B. Minster (1995), GPS detection of ionospheric perturbations following the January 17, 1994, Northridge earthquake, *Geophys. Res. Lett.*, *22*, 1045–1048, doi:10.1029/95GL00168.

Calais, E., and J. B. Minster (1996), GPS detection of ionospheric perturbations following a Space Shuttle ascent, *Geophys. Res. Lett.*, *23*, 1897–1900, doi:10.1029/96GL01256.

Calais, E., Haase, J. S., and Minster, J. B. (2003), Detection of ionospheric perturbations using a dense GPS array in Southern California, *Geophys. Res. Lett.*, *30*(12), 1628, doi:10.1029/2003GL017708.

Catherine, J. K., M. S. M. Vijayan, U. B. Syeda Rabiya, K. Shimna, V. K. Gahalaut, and D. S. Ramesh (2015), Dichotomy in mode propagation of coseismic ionospheric disturbance: Observations from April 11, 2012 Indian Ocean earthquake, *J. Geophys. Res. Space Physics*, *120*, 3854–3867, doi:10.1002/2014JA020621.

Davies, K. (1980), Recent progress in satellite radio beacon studies with particular emphasis on the ATS-6 radio beacon experiment, *Space Sci. Rev.*, *25*, 357–430.

Ding, F., W. Wan, T. Mao, M. Wang, B. Ning, B. Zhao, and B. Xiong (2014), Ionospheric response to the shock and acoustic waves excited by the launch of the Shenzhou 10 spacecraft, *Geophys. Res. Lett.*, *41*, 3351–3358, doi:10.1002/2014GL060107.

Dow, J. M., R. E. Neilan, and C. Rizos (2009), The International GNSS Service in a changing landscape of Global Navigation Satellite Systems, *J. Geod.*, *83*, 191–198, doi:10.1007/s00190-008-0300-3.

Ducic, V., J. Artru, and P. Lognonne (2003), Ionospheric remote sensing of the Denali earthquake Rayleigh surface waves, *Geophys. Res. Lett.*, *30*(18), 1951–1954, doi:10.1029/2003GL017812.

Heki, K. (2011), Ionospheric electron enhancement preceding the 2011 Tohoku-Oki earthquake, *Geophys. Res. Lett.*, *38*, L17312, doi:10.1029/2011GL047908.

Heki, K., and J. Ping (2005), Directivity and apparent velocity of the coseismic ionospheric disturbances observed with a dense GPS array, *Earth Planet. Sci. Lett.*, *236*, 845–855, doi:10.1016/j.epsl.2005.06.010.

Huang, Y. N., C. Kang, and S. W. Chen (1985), On the detection of acoustic gravity waves generated by typhoon by use of real time HF Doppler frequency shift sounding system, *Radio Sci.*, *20*, 897–906, doi:10.1029/RS020i004p00897.

Kherani, E. A., P. Lognonne, H. Hebert, L. Rolland, E. Astafyeva, G. Occhipinti, P. Coısson, D. Walwer, and E. R. de Paula (2012), Modelling of the total electronic content and magnetic field anomalies generated by the 2011 Tohoku-Oki tsunami and associated acoustic-gravity waves, *Geophys. J. Int.*, *191*, 1049–1066, doi:10.1111/j.1365-246X.2012.05617.x.

Landau, L. D., and E. M. Lifshitz (1995), *Fluid Mechanics, Course of Theoretical Physics*, vol. 6, 1st ed., Pergamon Press, Pergamon.

Larson, E. W., and G. Ekstrom (2001), Global models of surface wave group velocity, *Pure Appl. Geophys.*, *158*, 1377–1399.

Liu, J. Y., Y. B. Tsai, S. W. Chen, C. P. Lee, Y. C. Chen, H. Y. Yen, W. Y. Chang, and C. Liu (2006), Giant ionospheric disturbances excited by the *M*9.3 Sumatra earthquake of 26 December 2004, *Geophys. Res. Lett.*, *33*, L02103, doi:10.1029/2005GL023963.

Ma, Z., G. L. GuyMasters, and M. Pasyanos (2014), A comprehensive dispersion model of surface wave phase and group velocity for the globe, *Geophys. J. Int.*, *199*, 113–135, doi:10.1093/gji/ggu246.

Mitra, S., K. Priestley, V. K. Gaur, S. S. Rai, and J. Haines (2006), Variation of Rayleigh wave group velocity dispersion and seismic heterogeneity of the Indian crust and uppermost mantle, *Geophys. J. Int.*, *164*, 88–98, doi:10.1111/j.1365-246X.2005.02837.x.

Occhipinti, G., P. Dorey, T. Farges, and P. Lognonné (2010), Nostradamus: The radar that wanted to be a seismometer, *Geophys. Res. Lett.*, *37*, L18104, doi:10.1029/2010GL044009.

Ogawa, T., N. Nishitani, T. Tsugawa, and K. Shiokawa (2012), Giant ionospheric disturbances observed with the SuperDARN Hokkaido HF radar and GPS network after the 2011 Tohoku earthquake, *Earth Planets Space*, *64*, 1295–1307.

Otsuka, Y., et al. (2006) GPS detection of total electron content variations over Indonesia and Thailand following the 26 December 2004 earthquake, *Earth Planets Space*, *58*, 159–165.

Ozeki, M., and K. Heki (2010), Ionospheric holes made by ballistic missiles from North Korea detected with a Japanese dense GPS array, *J. Geophys. Res.*, *115*, A09314, doi:10.1029/2010JA015531.

Paul, A., A. Das, and A. Das Gupta (2011), Characteristics of SBAS grid sizes around the northern crest of the equatorial ionization anomaly, *J. Atmos. Sol. Terr. Phys.*, *73*, 1715–1722.

Perevalova, N. P., V. A. Sankov, E. I. Astafyeva, and S. Zhupityaeva (2014), Threshold magnitude for ionospheric TEC response to earthquakes, *J. Atmos. Terr. Phys.*, *1–8*, 77–90.

Pulinets, S. (2004), Ionospheric precursors of earthquakes; Recent advances in theory and practical applications, *Terr. Atmos. Oceanic Sci.*, *15*, 413–435.

Rama Rao, P. V. S., S. Gopi Krishna, K. Niranjan, and D. S. V. V. D. Prasad (2006), Study of spatial and temporal characteristics of L-band scintillations over the Indian low-latitude region and their possible effects on GPS navigation, *Ann. Geophys.*, *24*, 1567–1580.

Rolland, L. M., P. Lognonné, and H. Munekane (2011a), Detection and modeling of Rayleigh wave induced patterns in the ionosphere, *J. Geophys. Res.*, *116*, A05320, doi:10.1029/2010JA016060.

Rolland, L. M., P. Lognonne, E. Astafyeva, E. A. Kherani, N. Kobayashi, M. Mann, and H. Munekane (2011b), The resonant response of the ionosphere imaged after the 2011 off the Pacific coast of Tohoku earthquake, *Earth Planets Space*, *63*, 853–857.

Row, R. V. (1967), Acoustic-gravity waves in the upper atmosphere due to a nuclear detonation and an earthquake, *J. Geophys. Res.*, *72*, 1599–1610, doi:10.1029/JZ072i005p01599.

Ryu, K., E. Lee, J. S. Chae, M. Parrot, and S. Pulinets (2014), Seismo-ionospheric coupling appearing as equatorial electron density enhancements observed via DEMETER electron density measurements, *J. Geophys. Res. Space Physics*, *119*, 8524–8542, doi:10.1002/2014JA020284.

Sagiya, T. (2004), A decade of GEONET: 1994–2003—The continuous GPS observation in Japan and its impact on earthquake studies, *Earth Planets Space*, *56*, 29–41.

Saito, A., T. Tsugawa, Y. Otsuka, M. Nishioka, T. Iyemori, M. Matsumura, S. Saito, C. H. Chen, Y. Goi, and N. Choosakul (2011), Acoustic resonance and plasma depletion detected by GPS total electron content observation after the 2011 off the Pacific coast of Tohoku earthquake, *Earth Planets Space*, *63*, 863–867.

Sardón, E., and N. Zarraoa (1997), Estimation of total electron content using GPS data: How stable are the differential satellite and receiver instrumental biases?, *Radio Sci.*, *32*(5), 1899–1910, doi:10.1029/97RS01457.

Seemala, G. K., and C. E. Valladares (2011), Statistics of total electron content depletions observed over the South American continent for the year 2008, *Radio Sci.*, *46*, RS5019, doi:10.1029/2011RS004722.

Sunil, A. A., M. S. Bagiya, C. D. Reddy, M. Kumar, and D. D. Ramesh (2015), Post-seismic ionospheric response to the 11 April 2012 East Indian Ocean doublet earthquake, *Earth Planets Space*, *67*, 37, doi:10.1186/s40623-015-0200-8.

Tsugawa, T., A. Saito, Y. Otsuka, M. Nishioka, T. Maruyama, H. Kato, T. Nagatsuma, and K. T. Murata (2011), Ionospheric disturbances detected by GPS total electron content observation after the 2011 off the Pacific coast of Tohoku earthquake, *Earth Planets Space*, *63*, 875–879.

Valladares, C. E., J. Villalobos, M. A. Hei, R. Sheehan, S. Basu, E. MacKenzie, P. H. Doherty, and V. H. Rios (2009), Simultaneous observation of travelling ionospheric disturbances in the Northern and Southern Hemispheres, *Ann. Geophys.*, *27*, 1501–1508, doi:10.5194/angeo-27-1501-2009.

Yagi, Y., and R. Okuwaki (2015), Integrated seismic source model of the 2015 Gorkha, Nepal, earthquake, *Geophys. Res. Lett.*, doi:10.1002/2015GL064995.